

CASCO: Cosmological and Astrophysical parameters from Cosmological simulations and Observations

III. The physics behind the emergence of the golden mass scale

C. Tortora,^{1*} V. Busillo,^{1,2,3} N. R. Napolitano,² L. V. E. Koopmans,⁴ G. Covone,^{2,3} S. Genel,^{5,6} F. Villaescusa-Navarro,^{5,7} M. Silvestrini^{1,2}

¹INAF – Osservatorio Astronomico di Capodimonte, Salita Moiariello 16, I-80131, Napoli, Italy

²Dipartimento di Fisica “E. Pancini”, Università degli studi di Napoli Federico II, Compl. Univ. di Monte S. Angelo, Via Cintia, I-80126 Napoli, Italy

³INFN, Sez. di Napoli, Compl. Univ. di Monte S. Angelo, Via Cintia, I-80126 Napoli, Italy

⁴Kapteyn Astronomical Institute, University of Groningen, P.O Box 800, 9700 AV Groningen, The Netherlands

⁵Center for Computational Astrophysics, Flatiron Institute, 162 5th Avenue, New York, NY 10010, USA

⁶Columbia Astrophysics Laboratory, Columbia University, 550 West 120th Street, New York, NY 10027, USA

⁷Department of Astrophysical Sciences, Princeton University, 4 Ivy Lane, Princeton, NJ 08544 USA

February 20, 2025

ABSTRACT

Studies using photometric and spectroscopic data have suggested the emergence of characteristic physical mass scales, such as the so-called golden mass, corresponding to a virial mass of approximately $10^{12} M_{\odot}$ and a stellar mass of approximately $5 \times 10^{10} M_{\odot}$. This mass scale marks a bend in the halo-to-stellar mass relation, indicating a maximum in star formation efficiency, where galaxies are minimally affected by processes like supernovae (SN) and Active Galactic Nuclei (AGN) feedback. We use CAMELS cosmological simulations within a volume equal to $(50 h^{-1} \text{ Mpc})^3$, based on the IllustrisTNG subgrid, to study the origin of this mass scale and whether it persists when varying feedback from SN and AGN, as well as the cosmological parameters Ω_m and σ_8 , across cosmic time. We focus on the correlation between the total-to-stellar mass within the half-mass radius and stellar mass, which follows an inverted bell-shaped trend, with a minimum at the golden mass. The cosmological parameters affect the normalization of the scaling relation but not the emergence of the golden mass. SN feedback processes impact both the normalization and the emergence of the golden stellar mass, which shifts to lower mass for high values of wind velocity and energy. We examine eight AGN feedback parameters and find that most influence the emergence of the golden mass, altering the correlation slope at high mass: the black hole radiative efficiency, i.e. the fraction of the accretion rest mass released in the accretion process, is the most impactful, followed by the black hole feedback factor (normalization factor for the energy in the AGN feedback) and quasar threshold (i.e. the Eddington ratio). When the sample is investigated in terms of galaxy types, ETGs preserve the inverted bell-shaped trend, while LTGs have monotonically decreasing DM fractions with mass, with mild indication of an inversion only at low redshift, confirming some recent results from observations. When connecting with global quantities, we see that stellar fraction (and consequently the star formation efficiency) show a bell-shaped trend peaking at the golden mass, with behaviours that mirror the central quantities. When galaxy types are considered, the golden mass in ETGs vanishes, and a peak at lower mass is seen, while LTGs mirror the behaviour in the central quantity, with mild indication of a maximum in the stellar fraction only at low redshift. Overall, we find that the emergence of the golden mass is driven by the SN- and AGN-related feedback and appears earlier in cosmic time for stronger-feedback simulations, which faster quench star formation in the most massive galaxies.

Key words. Galaxies: formation, Galaxies: evolution, dark matter, Methods: numerical

1. Introduction

Research using spectroscopic and photometric data have led to the characterization of scaling relations among various galaxy parameters, including stellar populations (age, metallicity, luminosity, stellar mass, IMF slope), structural properties (such as galaxy size and light profile), and total mass and dark matter (DM) distribution (DM fraction, mass density slope). Understanding the origins of these scaling relations, the physical processes shaping them and their role in galaxy evolution across a vast range of masses and cosmic time is central to modern stud-

ies of galaxy evolution (e.g., Courteau et al. 2014; D’Onofrio et al. 2021).

There is growing evidence that a critical stellar mass scale exists around $\sim 5 \times 10^{10} M_{\odot}$, corresponding to $\sim 10^{12} M_{\odot}$ in virial mass (e.g. Dekel & Birnboim 2006). This mass scale appears as transitions, breaks, or extrema in the trends of various scaling relations. Given the power-law nature of the DM power spectrum from simulations (Widrow et al. 2009), there is no reason to consider any particular mass scale as special. In contrast, the stellar mass function follows a Schechter form. As a result, near the break of the stellar mass function, star formation efficiency reaches its peak, whereas at both higher and lower mass scales, feedback mechanisms reduce this efficiency. Thus, any charac-

* E-mail: crescenzo.tortora@inaf.it

teristic mass scale is likely tied to baryonic processes rather than DM dynamics.

This characteristic mass, often referred to as the "golden mass" (or "transition mass" or "bimodality mass"), is observed in several contexts, including the trends of total mass-to-light ratio and star formation efficiency with galaxy mass when considering all galaxies (e.g., Benson et al. 2000; Marinoni & Hudson 2002; van den Bosch et al. 2007; Conroy & Wechsler 2009; Moster et al. 2010; Girelli et al. 2020). Differences, however, emerge when different galaxy types are considered (e.g., Dutton et al. 2010; More et al. 2011; Wojtak & Mamon 2013; Posti et al. 2018; Correa & Schaye 2020). The golden mass also manifests in the half-light dynamical M/L and DM fraction (Wolf et al. 2010; Toloba et al. 2011; Cappellari et al. 2013; Tortora et al. 2016, 2019; Lovell et al. 2018; Busillo et al. 2023), in the gradients of dynamical M/L profiles across several effective radii (Napolitano et al. 2005), and in the total mass density slope of galaxies (Tortora et al. 2019). Historically, this mass scale has also emerged from structural analyses, such as the correlation between effective surface brightness and effective radius (Capaccioli et al. 1992, Tully & Verheijen 1997, Kormendy et al. 2009) and size-mass relations (Shen et al. 2003; Hyde & Bernardi 2009; Tortora et al. 2009), as well as in trends of optical color, metallicity, and stellar M/L gradients (Kuntschner et al. 2010; Spolaor et al. 2010; Tortora et al. 2010, 2011). This extensive body of empirical evidence consistently converges on a value for the golden stellar mass around $3 - 5 \times 10^{10} M_{\odot}$.

If this is indeed a fundamental mass scale in galaxy formation and evolution, it is plausible that the physical processes driving galaxy evolution also change when crossing this mass threshold. One well-studied scaling relation involves total virial mass and stellar mass, which can be translated into a relation between the stellar fraction (the ratio of stellar to virial mass) and stellar or virial mass (e.g. Moster et al. 2010). When the stellar fraction is normalized by the cosmological baryon fraction, the star formation efficiency is defined. The bending observed in the virial-to-stellar mass relation translates into a peak in the correlation between stellar fraction (or star formation efficiency) and mass at the golden mass. Analyzing the correlation between stellar fraction or star formation efficiency with mass can provide insights into the role of various galactic processes, for example SN and AGN feedback, which are believed to dominate at low and high masses, respectively. At the golden mass, supernova-driven winds and AGN feedback become less effective at depleting the galaxy's gas supply and quenching star formation (e.g., Dekel & Birnboim 2006; Moster et al. 2010). Moreover, Dekel & Birnboim (2006) have proposed that the primary driver of the bimodality in galaxy properties is the transition from cold gas inflows to virial shock heating at a critical virial mass scale of $\sim 10^{12} M_{\odot}$, in conjunction with feedback processes and gravitational clustering.

However, tensions arise when considering different galaxy types. A bending in the trend of star formation efficiency with mass is not seen in recent analyses of rotation curves of star-forming galaxies, pointing to larger star formation efficiencies of late-type systems when compared to early-types of similar mass above the golden mass (Posti et al. 2018). Building stellar-to-halo mass relations through statistical approaches that combine various semi-empirical methods of galaxy-halo connection, Rodríguez-Puebla et al. (2015) found a segregation in color for central galaxies, with bluer galaxies having a larger stellar fraction than red galaxies at fixed virial mass. Using SDSS data with visual classifications, Correa & Schaye (2020) found that disks have stellar masses (and hence star formation efficiencies) that

are larger or equal to those of ellipticals at virial masses below $10^{13} M_{\odot}$, and less massive at larger virial masses; EAGLE simulations also indicate that disks are more massive than ellipticals at fixed virial mass. In contrast to Posti et al. (2018), both studies observed the golden mass in both galaxy types. When the same quantities are calculated in the central galactic regions and transformed into a DM fraction within the half-light radius, early-type galaxies (ETGs) exhibit a bell-shaped trend (Tortora et al. 2016, 2019). Using the same data as in Posti et al. (2018), Tortora et al. (2019) only found some mild evidence of a bending in such scaling relations for late-type galaxies (LTGs).

Understanding the nature of the golden mass is therefore a central question to unravelling the physical processes governing galaxy formation. Despite progress, the physics underlying these scaling relations remains unclear, leaving key questions: What processes shape the observed scaling relations, and to what extent? Why does the golden mass emerge, and how does it manifest? How do these relations and the golden mass vary with cosmic time and galaxy types? These questions can be addressed by exploring the predictions of cosmological simulations and comparing them with observations (e.g. Mukherjee et al. 2018, 2021, 2022; Busillo et al. 2023).

We began exploring these issues in the first two papers of the "Cosmological and Astrophysical parameters from Cosmological simulations and Observations" (CASCO) series, using CAMELS simulations within a volume of $(25 h^{-1} \text{ Mpc})^3$, one of the most advanced suites of cosmological simulations, which allows for variation in cosmological parameter values and, most relevantly for this paper, the strength of SN and AGN feedback (Villaescusa-Navarro et al. 2021, 2022; Ni et al. 2023). By identifying the best simulations that reproduce different observed scaling relations among central DM mass and fraction, total virial mass, and half-mass radius versus stellar mass for different data samples (for both ETGs and LTGs) in Busillo et al. (2023, Paper I hereafter) and Busillo et al. (2024, Paper II hereafter), we have constrained cosmological and astrophysical parameters.

In this third paper of the CASCO series, we address the aforementioned open questions from a theoretical point of view, focusing on the origin of the golden mass, using the latest CAMELS simulations, which improve the galaxy count statistics by increasing the simulation volume eightfold to $(50 h^{-1} \text{ Mpc})^3$. We examine the scaling relations between the total-to-stellar mass ratio within the half-mass radius and stellar mass, as well as the correlation between half-mass radius and stellar mass, and total stellar mass fraction and stellar mass, as a function of redshift to decipher the impact of SN and AGN feedback. The quantification of the golden mass value is based exclusively on simulations, with the goal of assessing the influence of cosmological parameters and SN/AGN feedback. Comparisons with observational data are discussed in our previous publications (Papers I and II) and will be further addressed in future works.

The paper is organized as follows. In Section 2, we present the simulations. Results on the effect of astrophysical and cosmological parameters on the scaling relations and the golden mass are discussed in Section 3, and a summary of the results with future prospects is provided in Section 4.

2. Data

Following Papers I and II, we use the simulated galaxy data coming from CAMELS, a suite of cosmological simulations, originally within a cosmological volume of $(25 h^{-1} \text{ Mpc})^3$ (Villaescusa-Navarro et al. 2021, 2022; Ni et al. 2023). In this paper, we also

Table 1. List of free parameters of CAMELS simulations used in this paper. See more details in Ni et al. (2023).

Parameter	Description
Ω_m	cosmological mass density parameter
σ_8	rms of the $z = 0$ linear overdensity in spheres of radius $8 h^{-1}$ Mpc
A_{SN1}	normalization factor for the energy in galactic winds per unit star formation
A_{SN2}	normalization factor for the galactic wind speed
A_{AGN1}	radio feedback factor, i.e., normalization factor for the energy in AGN feedback, per unit accretion rate
A_{AGN2}	radio feedback reorientation factor, i.e., normalization factor for the frequency of AGN feedback energy release events
BH_{accr}	BH accretion factor, i.e., normalization factor for the Bondi rate for the accretion onto BHs
BH_{Edd}	BH Eddington factor, i.e., normalization factor for the limiting Eddington rate for the accretion onto BHs
BH_{FF}	BH feedback factor, i.e., normalization factor for the energy in AGN feedback, per unit accretion rate
BH_{RE}	BH radiative efficiency, i.e., the fraction of the accretion rest mass that is released in the accretion process
Q_T	Quasar threshold, i.e., the Eddington ratio, that serves as the threshold between the low-accretion and high-accretion states of AGN feedback
Q_{TP}	Quasar threshold power, i.e., the power-law index of the scaling relation of the low- to high-accretion state threshold with BH mass

Table 2. Values of the '1P' simulation parameters listed in Table 1.

Parameter	Variations				
	n2	n1	fiducial	p1	p2
Ω_m	0.1	0.2	0.3	0.4	0.5
σ_8	0.6	0.7	0.8	0.9	1
A_{SN1}	0.9	1.8	3.6	7.2	14.4
A_{SN2}	3.7	5.2	7.4	10.5	14.8
A_{AGN1}	0.25	0.5	1	2	4
A_{AGN2}	10	14.1	20	28.3	40
BH_{accr}	0.25	0.5	1	2	4
BH_{Edd}	0.1	0.32	1	3.2	10
BH_{FF}	0.025	0.05	0.1	0.2	0.4
BH_{RE}	0.05	0.1	0.2	0.4	0.8
Q_T	6.33×10^{-5}	3.6×10^{-4}	0.002	0.011	0.063
Q_{TP}	0	1	2	3	4

¹ The parameter values are labeled as n2, n1, fiducial, p1, and p2, ranging from the lowest to the highest. In the figures, for the astrophysical parameters, values are normalized relative to the fiducial simulation.

¹ Each row in the table corresponds to a 1P simulation set, where the parameter in the first column is varied while the others remain fixed.

use a new suite of simulations, where the Universe volume is increased by eight times to $(50 h^{-1} \text{ Mpc})^3$. The specific details of the simulations, other than the volume, are already described in detail in Paper I and II. Each simulation has the following cosmological parameter values fixed: $\Omega_b = 0.049$, $n_s = 0.9624$ and $h = 0.6711$. We will limit to the CAMELS simulations based on the IllustrisTNG subgrid physics. The masses and radii of the galaxies investigated in this paper significantly exceed particle mass resolutions and softening length, respectively.

The fiducial CAMELS simulation uses the same parameters of IllustrisTNG, which is calibrated to observations. These calibrations have been performed by using the galaxy stellar mass function, the stellar-to-halo mass relation, the total gas mass content within the virial radius r_{500} of massive groups, the stellar size - stellar mass and the black hole (BH) mass - galaxy mass relations, all at $z = 0$, and, finally, the functional shape of the cosmic star formation rate density for $z \lesssim 10$ (Pillepich et al. 2018).

With respect to the original CAMELS suites, which allowed for the variation of only six parameters, the updated set of simulations allows us to explore the role of 28 astrophysical and cosmological parameters in total. In particular, we vary the two cosmological parameters (Ω_m , σ_8), the originally implemented SN- and AGN-feedback parameters (A_{SN1} , A_{SN2} , A_{AGN1} , and A_{AGN2}) and six more parameters regulating AGN feedback. In particular, A_{SN1} and A_{SN2} are related to the SN feedback mechanisms, wind energy and velocity, respectively. Instead, A_{AGN1} and A_{AGN2} are the normalization factors of energy and frequency of AGN feedback (Villaescusa-Navarro et al. 2021). However, previous pa-

pers have demonstrated that A_{AGN1} and A_{AGN2} have no effect on scaling relations (see for example Papers I and II), and therefore we only investigate the impact of the six other AGN feedback parameters, which have been implemented in the latest CAMELS release. The complete list of parameters we will consider in this paper are listed in Table 1. We use the so called '1P' simulations, where we can vary one of the parameters at a time, holding the rest of the parameters constant (e.g., Villaescusa-Navarro et al. 2021). The values of the simulation parameters varied in each '1P' simulation set (including the fiducial simulation ones) are listed in Table 2. In the rest of the paper, astrophysical parameter values are normalized to the parameter value of the fiducial simulation, which corresponds to the unit value in our figures.

Differently from our previous papers, where we analyzed different scaling relations, comparing simulations with observations, in the present paper we will only use the simulations and mostly the scaling relation $M_{tot,1/2}/M_{*,1/2}$ vs M_* (or M_{tot}), where $M_{tot,1/2}$ and $M_{*,1/2}$ are the 3D total (including DM, stars and gas) and stellar mass calculated within the 3D stellar half-mass radius, respectively, M_* is the total stellar mass¹, and M_{tot} is the total (virial) mass. For completeness, and for connecting the central galaxy regions to the whole galaxy, we also investigate the correlation between the total stellar fraction M_*/M_{tot} and stellar mass. We explore how these scaling relations are varying as a function of redshift, using simulations at the following redshift slices: 0, 0.5, 1.0, 1.5 and 2.

Similarly to the previous work, we performed a filtering of the subhalos detected by SUBFIND. We considered only subhalos that have $R_{*,1/2} > \epsilon_{min}$, $N_{*,1/2} > 50$ and $f_{DM}(< R_{*,1/2}) \equiv 1 - M_{*,1/2}/M_{tot,1/2} > 0$, where $\epsilon_{min} = 2$ ckpc is the gravitational softening length of the IllustrisTNG suite. The selection criteria on $R_{*,1/2}$ and $N_{*,1/2}$ prevent strong resolution biases.

Similarly to Paper I and II, we follow Bisigello et al. (2020) for the selection of ETGs and LTGs via specific SFR (sSFR := SFR/ M_*), choosing for the ETGs only subhalos having $\log_{10}(\text{sSFR}/\text{yr}^{-1}) < -10.5$, and the opposite for LTGs. We have verified that varying the sSFR threshold by ± 0.5 dex does not affect our results (see Paper I).

The key observables from the simulations used in this paper are listed in Table 3.

3. The golden mass

Using the same parameters of the reference IllustrisTNG, calibrated, among other factors, to the observed $z = 0$ size-stellar

¹ We limit the analysis to a Chabrier (2003) IMF, deferring the investigation of the IMF's impact on stellar mass and DM fraction to a future paper (see more on the IMF in Tortora et al. 2009, 2013).

Table 3. Observables used in the paper.

Observable	Description
$R_{\star,1/2}$	half-mass radius
M_{\star}	stellar mass
M_{tot}	total mass
$M_{\text{tot},1/2}$	total mass within $R_{\star,1/2}$
$M_{\star,1/2}$	stellar mass within $R_{\star,1/2}$
$N_{\star,1/2}$	number of particles within $R_{\star,1/2}$
SFR	current star formation rate

mass and halo-to-stellar mass relations, the fiducial CAMELS simulation reveals a bending in the simulated size-stellar mass and halo-to-stellar mass relations around a mass of approximately $5 \times 10^{10} M_{\odot}$ (see also Paper I and II). This mass scale is transferred, for example, into the correlation among $M_{\text{tot},1/2}/M_{\star,1/2}$ and M_{\star} and any other related scaling relation. Therefore this feature and the specific shape of these observed scaling relations are naturally and by construction introduced during the calibration of the reference simulation. However, since this calibration is not transferred to the other simulations with varied parameters, the scaling relations are no longer primarily influenced by the initial calibration. While the calibration process prevents a fully agnostic analysis of the emergence of the golden mass scale, it firmly enables us to assess the impact of cosmology and astrophysical processes on the shape of the scaling relations, as well as the emergence and value of the golden mass over cosmic time.

One significant limitation of the CAMELS simulations is the relatively small cosmological volume, which restricts the number of massive objects, especially in the mass range where the golden mass is expected to appear. However, compared to the original CAMELS simulations, which simulate a volume of $(25 h^{-1} \text{Mpc})^3$, the current suite increases the volume, resulting in a galaxy count eight times larger. This increase in sample size is particularly important in the high-mass range ($M_{\star} > 5 \times 10^{10} M_{\odot}$), where galaxies are less abundant, as it facilitates the determination of the golden mass.

To estimate the golden mass as a function of the simulation parameters, for each simulation we fit a parabola to the simulation data in the vicinity of the minimum in the scaling relation. The results for the $z = 0$ snapshot are summarized in Table 4. The typical uncertainty in the (log) golden mass is approximately 0.1 – 0.2 dex.

3.1. Golden stellar mass

We investigate the impact of the twelve simulation parameters listed in Table 1 on the $M_{\text{tot},1/2}/M_{\star,1/2}-M_{\star}$ scaling relation in Figs. 1, 2 and 3. Following the results presented in Paper II, for most of the simulations a bell-shaped curve, with a minimum at the golden stellar mass, is observed. In particular, for the reference simulation, it takes the value of $\sim 5 \times 10^{10} M_{\odot}$. This result confirms what has been found combining observations for dwarf and giant ETGs and LTGs (Tortora et al. 2016, 2019) and not surprisingly results from Illustris TNG (Lovell et al. 2018).

3.1.1. Cosmological parameters

In Fig. 1, where only the cosmological parameters are varied, and the rest of parameters are fixed to the values of the fiducial simulations, we show that the impact of Ω_m on the scaling relation is more significant than that of σ_8 (reconfirming the findings reported in Papers I and II). Higher values of both parameters re-

Table 4. Golden mass estimates in $\log M_{\star}/M_{\odot}$, at $z = 0$. The uncertainty on the estimated values is $\sim 0.1 - 0.2$ dex.

Parameter	Variations					Trend
	n2	n1	fiducial	p1	p2	
Ω_m	10.8	10.7	10.7	10.7	10.8	\approx
σ_8	10.6	10.7	10.7	10.7	10.8	\approx
A_{SN1}	10.8	10.8	10.7	10.6	10.5	↓
A_{SN2}	11.1	10.9	10.7	10.6	10.5	↓↓
A_{AGN1}	10.8	10.7	10.7	10.7	10.7	\approx
A_{AGN2}	10.7	10.7	10.7	10.7	10.7	\approx
BH_{accr}	-	10.9	10.7	10.6	10.7	↓
BH_{Edd}	-	-	10.7	10.7	10.7	\approx
BH_{FF}	10.6	10.5	10.7	10.9	11.1	↑↑
BH_{RE}	10.3	10.5	10.7	11.1	-	↑↑↑
Q_{T}	11.1	10.9	10.7	10.6	10.5	↓↓
Q_{TP}	-	10.9	10.7	10.6	10.6	↓

¹ The parameter values corresponding to n2, n1, fiducial, p1, and p2, are listed in Table 2.

² The direction of the trend is shown in the last column, using the following symbols: \approx indicates no statistically significant trend, ↓ and ↑ represent negative and positive correlations, respectively, while double or triple arrows denote stronger correlations.

sult in galaxies with greater DM content, although their impact on the golden mass appears negligible. We observe only a very mild flattening at the high-mass end for the largest σ_8 values. In general, we observe that the minimum in the scaling relation begins to emerge between $z = 1.5$ and $z = 1$, becoming definitively established around $z = 0.5$.

3.1.2. SN feedback parameters

In Fig. 2 we show the impact of SN feedback, by limiting the analysis to the two parameters A_{SN1} and A_{SN2} , which determine the amplitude of the SN wind energy per unit star formation rate and the wind velocity, respectively. These are among the most influential parameters.

Consistent with findings in Papers I and II, we confirm that the SN energy per unit SFR parameter (A_{SN1}) is one of the most significant astrophysical parameters affecting our scaling relation (Paper I). Specifically, stronger wind energy corresponds to higher values of $M_{\text{tot},1/2}/M_{\star,1/2}$ at a fixed stellar mass. We can now also quantify the effect on the golden mass scale and the steepness of the scaling relation at masses below and above this scale. Notably, for low wind energy values, the bending is mild, and the golden mass becomes more pronounced as this parameter increases, becoming particularly well-defined for very strong wind energy. While the slope of the correlation at masses below the golden mass remains almost constant, the correlation for massive galaxies — dominated by ETGs — becomes increasingly steeper as a function of wind energy. In the simulation with the strongest wind energy ($A_{\text{SN1}} = 4$), the minimum—and thus the golden mass—occurs at $z \sim 1.5$. In contrast, simulations with weaker wind energy show that the minimum occurs at lower redshifts, with most models only revealing it at $z \sim 0$. In particular, at $z = 0$, we observe a decrease in the golden mass as A_{SN1} increases, dropping from $7 \times 10^{10} M_{\odot}$ to $3 \times 10^{10} M_{\odot}$.

The impact of the wind velocity amplitude, A_{SN2} , is more complex. At a fixed mass, as discussed in Paper II, the trend at high mass is similar to that of A_{SN1} , with larger values corresponding to higher DM content. However, the trend is reversed at lower masses, where LTGs dominate. Regarding the emergence

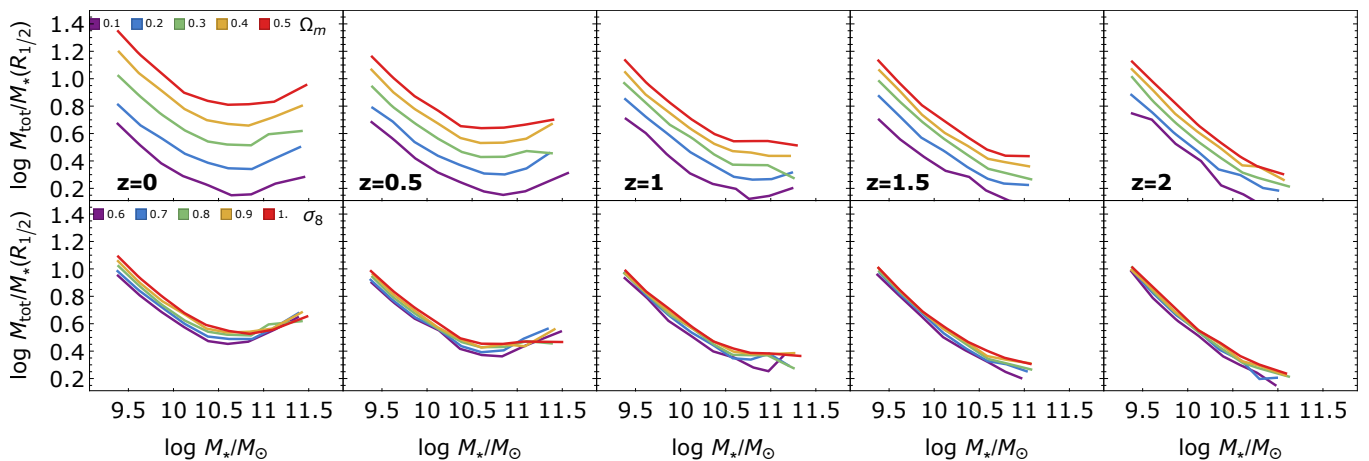


Fig. 1. The ratio $M_{\text{tot},1/2}/M_{*,1/2}$ is plotted against M_* for CAMELS simulations, with each row showing variations in the cosmological parameters Ω_m and σ_8 . The green lines represent the reference CAMELS simulation. To examine the evolution across redshift, simulation snapshots at $z = 0$, $z = 0.5$, $z = 1$, $z = 1.5$ and $z = 2$ are displayed from left to right. Medians in stellar mass bins are shown.

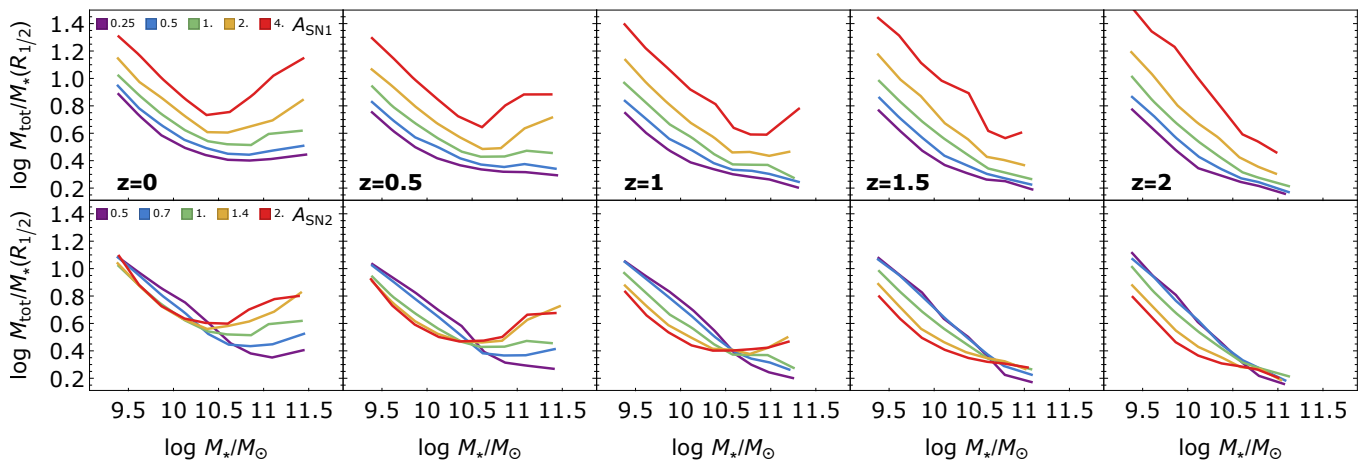


Fig. 2. The ratio $M_{\text{tot},1/2}/M_{*,1/2}$ is plotted against M_* for CAMELS simulations, with each row showing variations in the SN-related parameters A_{SN1} and A_{SN2} . The green lines represent the reference CAMELS simulation. To examine the evolution across redshift, simulation snapshots at $z = 0$, $z = 0.5$, $z = 1$, $z = 1.5$ and $z = 2$ are displayed from left to right. Medians in stellar mass bins are shown.

of the golden mass, similar to A_{SN1} , the bending in the scaling relation is almost absent for the lowest wind velocity values, with the golden mass appearing at around $10^{11} M_\odot$. The bending becomes stronger with increasing wind velocity. A stronger decrease in the golden mass value is observed with increasing A_{SN2} , ranging from approximately 10^{11} to $\sim 3 \times 10^{10} M_\odot$ for the extreme values of the parameter. When studying the correlations as a function of redshift, we find that a bend in the model with the highest wind velocity ($A_{\text{SN2}} = 2$) is already present at $z = 2$, but the minimum in the relation only emerges at $z = 1$. In most models with lower A_{SN2} values, the golden mass appears at $z \lesssim 0.5$.

3.1.3. AGN feedback parameters

The impact of eight parameters which regulate the AGN feedback in CAMELS simulations are finally investigated in Fig. 3.

As noted in our previous papers (see also Villaescusa-Navarro et al. 2022 and Chawak et al. 2023), the normalization factors for the energy and the frequency of events, i.e. A_{AGN1} and A_{AGN2} , have a negligible effect on scaling relations, which

we confirm for both the normalization of these relations and their impact on the golden mass scale. We only observe a minor effect on the slope of the trend in massive galaxies varying A_{AGN1} at $z < 0.5$.

In contrast, the impact of other AGN feedback parameters on the scaling relation is more significant, as it is expected to happen in the most massive galaxies, hosting super-massive BHs.

Larger values of the BH accretion factor BH_{accr} , BH Eddington factor BH_{Edd} , quasar threshold Q_T , and quasar threshold power Q_{TP} result in higher DM fractions at larger masses and introduce a bend in the scaling relation. For most of these parameters, and in simulations with their highest values, the golden mass is established around $z \sim 1$. For lower values of these parameters, the golden mass emerges at later redshifts. For BH accretion factor, quasar threshold, and quasar threshold power, larger golden mass values correspond to smaller parameter values. Focusing on the $z = 0$ snapshot, smaller values of BH_{accr} , i.e. smaller values for the normalization factor of the Bondi rate, push the golden mass to $\sim 10^{11} M_\odot$, while it remains nearly stable for values greater than or equal to the fiducial. For BH_{Edd} , models that show a clear minimum are those

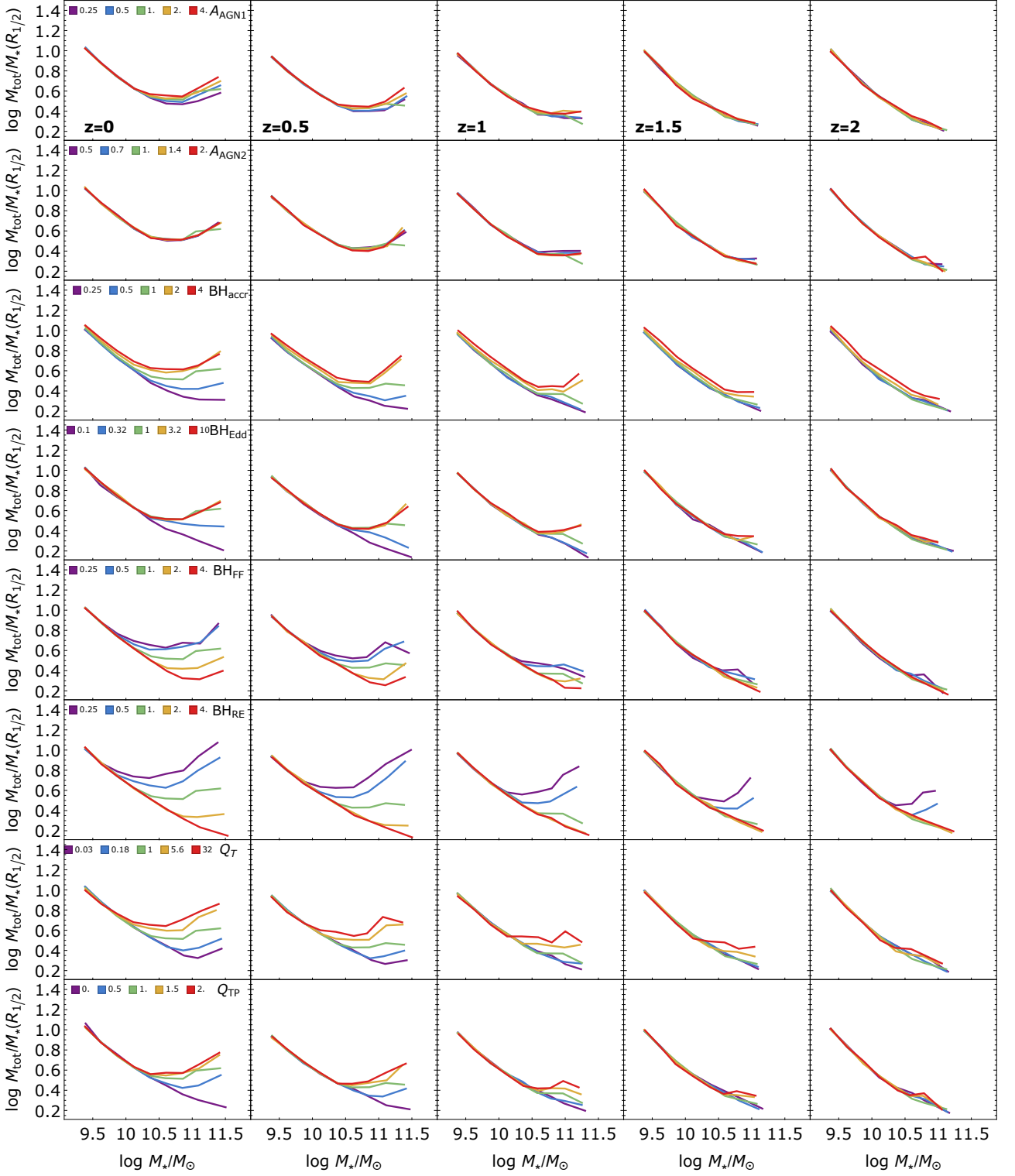


Fig. 3. The ratio $M_{\text{tot},1/2}/M_{*,1/2}$ is plotted against M_* , with each row showing variations in the AGN-related simulation parameters: A_{AGN1} , A_{AGN2} , BH_{accr} , BH_{Edd} , BH_{FF} , BH_{RE} , Q_T , and Q_{TP} from top to bottom. The green lines represent the reference CAMELS simulation. To examine the evolution across redshift, simulation snapshots at $z = 0$, $z = 0.5$, $z = 1$, $z = 1.5$ and $z = 2$ are displayed from left to right. Medians in stellar mass bins are shown.

with values \geq the fiducial, above which the golden mass stabilizes; therefore the normalization factor for the limiting Eddington rate is not impacting the golden mass value. Q_T regulates the threshold between the AGN feedback low- and high- accretion states, and is one of the parameters with the greatest impact on

the golden mass, reducing it from $10^{11} M_{\odot}$ in the weaker models to $3 \times 10^{10} M_{\odot}$ in the strongest models. Finally, the power-law index of the scaling relation of the low- to high-accretion state threshold with BH mass, i.e., the quasar threshold power (Q_{TP}),

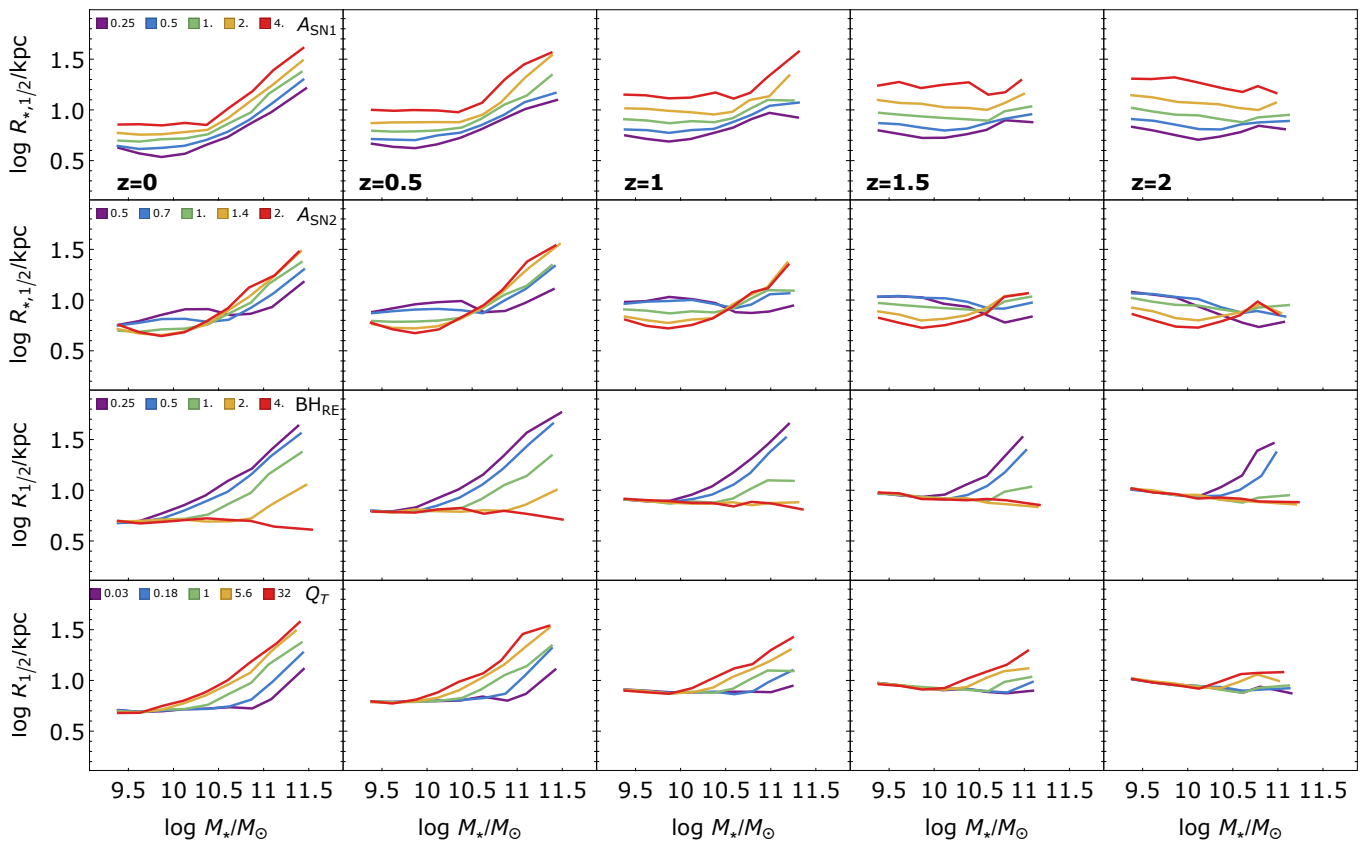


Fig. 4. The half-mass radius, $R_{*,1/2}$ is plotted against M_* , with rows showing variations in the two SN-related parameters A_{SN1} and A_{SN2} and two AGN parameters BH_{RE} and Q_{T} . The green lines represent the reference CAMELS simulation. Simulation snapshots at $z = 0$, $z = 0.5$, $z = 1$, $z = 1.5$ and $z = 2$ are displayed from left to right. Medians in virial mass bins are shown.

shows a bending trend starting from $Q_{\text{TP}} = 0.5$, with the golden mass and trends saturating for values \geq the fiducial simulation.

The opposite trend is observed for the BH feedback factor BH_{FF} , i.e. the normalization factor for the energy in AGN feedback, and the BH radiative efficiency BH_{RE} , corresponding to the fraction of accretion rest mass released in the accretion process. In these cases, larger parameter values correspond to smaller DM fractions compared to lower values. For the smallest values of BH_{RE} , the golden mass is already established at $z \sim 2$, while for larger values, it never appears. Regarding the BH feedback factor, the golden mass emerges across all models at $z < 1$. For both parameters, larger golden mass values correspond to larger parameter values. At $z = 0$, although the BH feedback factor BH_{FF} has a greater impact on DM normalization, the golden mass saturates at the lower end of the parameter range, increasing beyond the fiducial model up to $\sim 10^{11} M_{\odot}$ for the highest parameter values. Finally, the fraction of accretion rest mass that is released in the accretion process proves to be the most influential parameter. Indeed, for the weakest values of BH_{RE} , the golden mass is approximately $2 \times 10^{10} M_{\odot}$, whereas for the largest values, it exceeds $10^{11} M_{\odot}$.

3.1.4. The connection with the size-mass relation

We have seen that the golden mass is well defined and appears in earlier cosmic times in simulations with a stronger AGN and SN feedback, depending on the specific value of the parameters.

These effect can also be explained by a more rapid (or slower) size-mass evolution observed in these simulations.

By definition, the ratio $M_{\text{tot},1/2}/M_{*,1/2}$ depends on $R_{1/2}$, with larger DM fractions corresponding to larger $R_{1/2}$ values (e.g., Napolitano et al. 2010). We therefore, as an example, present this correlation in terms of A_{SN1} , A_{SN2} , BH_{RE} and Q_{T} in Fig. 4. The golden mass also emerges within these trends, although not as a minimum in the scaling relation, but as scale above which the scaling relation turns upward. At masses below the golden mass, the stellar half-mass radius remains nearly constant, while at larger masses, it becomes positively correlated with mass (except for the largest values of BH_{RE}), consistent with the trends observed in the data (see Papers I and II; e.g., Roy et al. 2018 and references therein). The trends with redshift indicate that galaxy sizes at lower masses (where LTGs dominate) mildly decrease over cosmic time, while sizes at higher masses (predominantly ETGs) increase. For massive galaxies, the increase of the size (and consequently of the central DM fraction) is faster for models with stronger feedback (higher wind energy and velocity, smaller BH_{RE} and higher Q_{T}), being the local size-mass relation already settled at earlier redshifts. The trends observed in relation to the SN-feedback parameters mirror those found for the central DM fraction in Fig. 2, where larger wind energies correspond to larger galaxy sizes. The characteristic bending associated with the golden mass is challenging to pinpoint, but it appears to be relatively unaffected. Since $M_{\text{tot},1/2}/M_{*,1/2}$ is positively correlated with $R_{1/2}$, the complex behavior noted in Fig. 2

concerning $A_{\text{SN}2}$ is also evident here: larger wind velocities lead to larger sizes at high masses and smaller sizes at lower masses. However, the impact of wind velocity on the golden mass seems consistent with that seen in DM fraction, with the bending occurring at smaller masses for higher wind velocities.

Interestingly, for both the correlations the golden mass is absent at $z = 2$ for any set of parameters, except for extreme values of the AGN-feedback parameters. It first emerges at $z \sim 1 - 1.5$ for high values of wind energy and velocity, and only at $z = 0$ for the lowest values of SN parameters. For extreme values of some AGN feedback parameters it emerges at $z \sim 2$, for other at lower redshifts, in some cases it never appears. As an example, it emerges at $z = 1.5 - 2$ only for the smallest values of BH_{RE} , and only at $z = 0$ for low values of BH_{accr} or Q_{T} and high values of BH_{RE} . This is suggesting a link to the quenching of galaxies. In all cases where the golden mass is observed, it becomes more consolidated over cosmic time. This emergence is also related to the behavior of the most massive galaxies, which begin to show a positive correlation between DM fraction and mass only between $z = 1$ and $z = 2$. Stronger feedback halts star formation, creating galaxies with smaller stellar masses and leading to a higher DM fraction. Star formation quenching and mergers contribute to the increase in size and DM fraction in the most massive galaxies over cosmic time. A more systematic analysis of the size-mass relation as a function of redshift, and the comparison with observations, are beyond the scope of this paper and will be analyzed in future papers.

3.2. Galaxy type dependency

Different types of galaxies are influenced by different processes and span different ranges of masses. Therefore, it is crucial to investigate whether scaling relations differ between these galaxy types. Figure 5 shows the relation between $M_{\text{tot},1/2}/M_{\star,1/2}$ and M_{\star} for ETGs and LTGs.

It is not surprising that the scaling relation for masses larger than the golden mass is predominantly driven by ETGs. This is because the number density of star-forming galaxies decreases significantly at $\sim 10^{10.5-11} M_{\odot}$. Additionally, due to our selection criterion of constant sSFR with redshift, the number of ETGs at $z = 2$ is notably low.

For any values of the parameters shown, the variation in central DM fraction with redshift is weaker for LTGs compared to ETGs. The stronger variation observed in ETGs is favoured by their greater size evolution. Except for the $z = 0$ snapshot, at fixed stellar mass, the DM fractions of LTGs are generally higher than those of ETGs. The impact of SN feedback parameters remains consistent when galaxy types are explicitly considered. The trends observed for the entire sample at high masses apply to ETGs, while some differences emerge at low masses and for LTGs.

In LTGs, the decreasing trend with M_{\star} of the DM fraction is confirming the results obtained with data both at low- and high- z (Tortora et al. 2019; Sharma et al. 2022). Although the number density of LTGs approaches zero at high masses, a slight change in slope and the emergence of the golden mass is observed for extreme values of some parameters². Some mild evidence of bending was found in Tortora et al. (2019), using SPARC star forming galaxies with measured rotation curves (Lelli et al. 2016), tending to exclude simulations with very extreme values of SN- and AGN-feedback parameters. However,

² In some panels, the same binning used across simulations obscures the detection of this bending.

the presence of the bend found in observations contrasts with findings in Posti et al. (2019), which, using the sample used in Tortora et al. (2019), reported (relying on global quantities) no bending in the relation between stellar fraction (of star formation efficiency) and stellar mass in the most massive spirals.

To resolve this discrepancy or at least discover the possible cause, it is important to examine the simulations' predictions for the total M_{\star}/M_{tot} , obtained including all particles in the subhalos. The results are presented in Fig. 6.

We confirm the maximum in the relation when all galaxies are considered (e.g., Moster et al. 2010), which mirrors the trends observed for central DM fraction as a function of stellar mass (e.g., Fig. 2). The peak of this relation, or the golden mass, increases with higher redshifts. In the highest redshift bin, we observe a flattening at high masses. Models with higher wind energy and velocity tend to have larger central DM fraction, and lower global stellar fractions M_{\star}/M_{tot} , indicating lower star formation efficiency. Similarly to Fig. 2, varying $A_{\text{SN}2}$ influences the golden mass, whereas $A_{\text{SN}1}$ less. Similitude with Fig. 3 can also be made by comparing the trends for AGN-feedback parameters shown in terms of scaling relation normalization and variation in the golden mass value.

For LTGs alone, indications of a golden mass are observed (although very weak), for example in models with high $A_{\text{SN}1}$ and Q_{T} values, which contradicts the findings of Posti et al. (2019). The absence of bending in the Posti et al. (2018) results would favour models with a weaker feedback. However, a larger volume would be beneficial to better sample the most massive end of the mass function where LTGs are extremely rare.

An interesting result pertains to the ETG population. When considering global quantities, the stellar fraction in our case, no clear bending at the golden mass is observed. Instead, there are mild indications of a peak at lower masses ($\sim 10^{9.5-10} M_{\odot}$), which increases for larger (smaller) values of, for example, BH_{RE} (Q_{T}). This contrasts with the analysis of the central quantities, where the golden mass clearly emerges for the whole sample and ETGs alone, driven by the bending observed in the size-mass relation in both samples (Fig. 5). This may be attributed to the fact that, on global scales, SN and AGN feedback have not yet had sufficient time to take effect. However, in future analyses, we will explore the origin of this result in greater detail.

4. Conclusions

In this paper, we investigated the emergence of the so-called "golden" mass, by studying the scaling relation between $M_{\text{tot},1/2}/M_{\star,1/2}$, the ratio of total-to-stellar mass within the half-mass radius (equivalent to a DM fraction), and stellar mass. We utilized a new suite of CAMELS simulations, which enhance previous simulations by increasing the volume to $(50 h^{-1} \text{Mpc})^3$, allowing for a more detailed examination of the most massive end of the galaxy mass function (Villaescusa-Navarro et al. 2021, 2022; Ni et al. 2023). These simulations enable us to analyze the impact of various astrophysical and cosmological parameters, including SN and AGN feedback strengths as well as Ω_m and σ_8 , across different redshifts. However, we note that larger volume simulations would be beneficial to determine whether a golden mass appears at masses greater than $10^{11} M_{\odot}$ at large redshifts.

For most astrophysical and cosmological parameter values across various redshifts, the $M_{\text{tot},1/2}/M_{\star,1/2}-M_{\star}$ relation follows an inverted bell-shaped curve, indicating the presence of a "golden mass" at the minimum of the curve (Tortora et al. 2019). However, at high redshifts, such as $z = 2$, this ratio decreases with stellar mass, and no golden mass is observed.

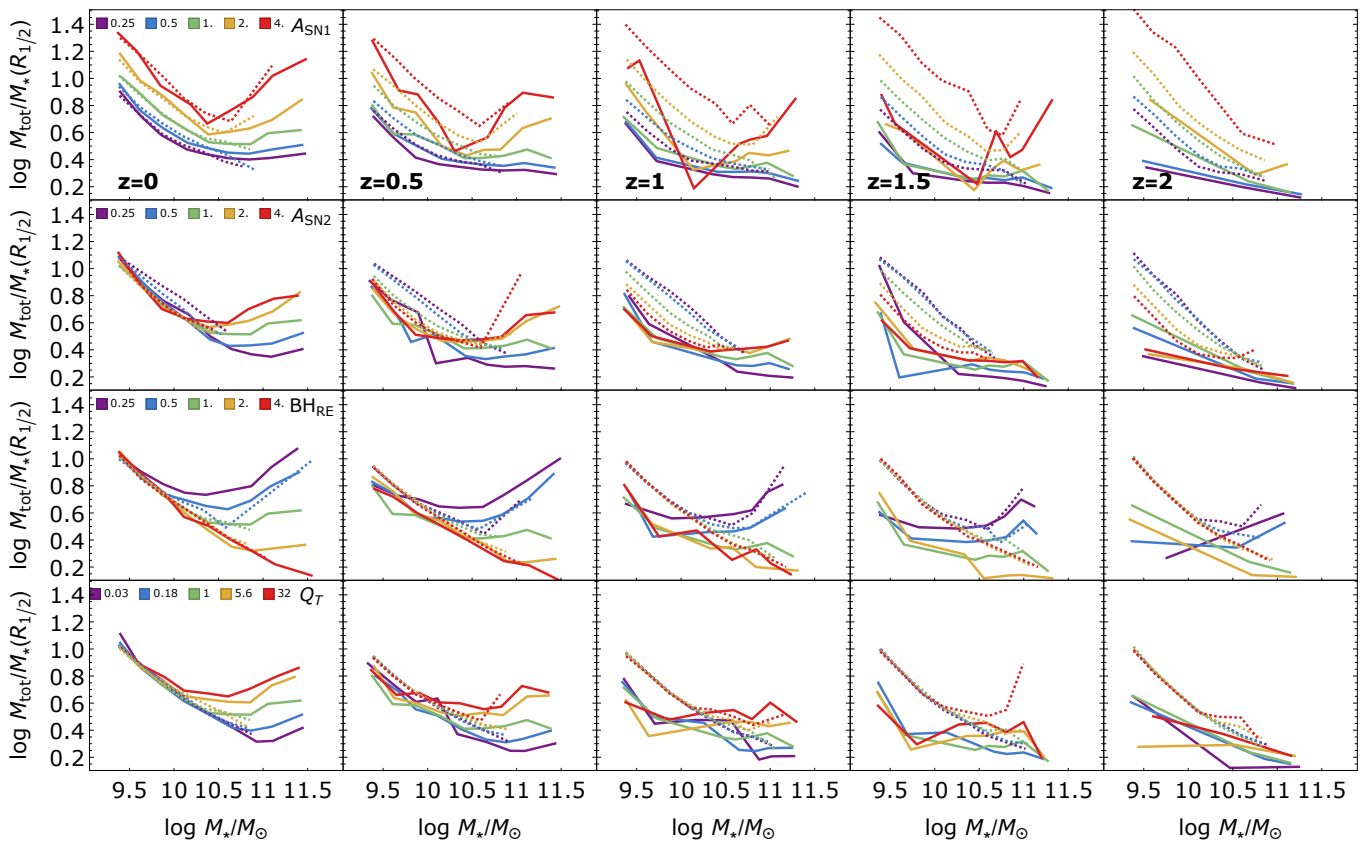


Fig. 5. The ratio $M_{\text{tot},1/2}/M_{*,1/2}$ is plotted against M_* , with rows showing variations in the two SN-related parameters A_{SN1} and A_{SN2} and the two AGN parameters B_{RE} and Q_T . The green lines represent the reference *CAMELS* simulation. Simulation snapshots at $z = 0$, $z = 0.5$, $z = 1$, $z = 1.5$ and $z = 2$ are displayed from left to right. The sample is divided in ETGs (solid lines) and LTGs (dashed lines). Medians in stellar mass bins are shown.

Cosmological parameters primarily influence the normalization of this scaling relation but do not affect the emergence of the golden mass. The inverted bell-shaped trend becomes more pronounced with higher values of supernova feedback energy (A_{SN1}) and wind velocity (A_{SN2}), with the latter having a stronger impact on the golden mass value. Our findings confirm that while the normalization factors for AGN energy and event frequency (A_{AGN1} and A_{AGN2}) have only minor or negligible effects on the scaling relations, other AGN feedback-related parameters implemented in the *CAMELS* simulations play a more significant role. Specifically, larger values of the normalization factor for the Bondi rate for the accretion onto BHs (BH accretion rate BH_{accr}), the normalization factor for the limiting Eddington rate for the accretion onto BHs (Eddington factor BH_{Edd}), the Eddington ratio, that serves as the threshold between the low-accretion and high-accretion states of AGN feedback (quasar threshold Q_T), and the power-law index of the scaling of the low- to high-accretion state threshold with BH mass (quasar threshold power Q_{TP}) increase DM fractions at high masses and induce a bend in the scaling relation, while factors such as the normalization factor for the energy in AGN feedback, per unit accretion rate (BH feedback factor BH_{FF}) and the fraction of the accretion rest mass that is released in the accretion process (BH radiative efficiency BH_{RE}) work in the opposite direction.

Summarizing, the fraction of the accretion rest mass that is released in the accretion process is the most impacting parameter on the golden mass value, followed by the normalization fac-

tor for the energy in AGN feedback, the threshold between the low-accretion and high-accretion states of AGN feedback and SN wind velocity, the rest of the parameters induce milder or absent trends.

In ETGs, the inverted bell-shaped curve is clearly visible in the $M_{\text{tot},1/2}/M_{*,1/2}-M_*$ relation, while LTGs display a monotonically decreasing trend with stellar mass across all redshifts, with only mild indications of a turnover at very low redshifts. These results align with observational findings (Tortora et al. 2016, 2019). In LTGs, DM fractions decrease over cosmic time, while ETGs show a significant increase, particularly in the most massive systems, where size evolution contributes to the rise in central DM fractions (e.g., Tortora et al. 2014, 2018). Models with stronger SN and AGN feedback demonstrate faster evolution in both size and DM fractions.

Regarding global quantities, LTGs, which dominate the scaling relation below the golden mass, exhibit only marginal bending, which becomes more pronounced with stronger wind energy. ETGs dominate at higher masses but do not show a sharp peak at the golden mass. Instead, they exhibit a mild peak around $10^{9.5-10} M_\odot$ (changing to larger values for extreme values of some AGN feedback parameters) and a decreasing trend at higher masses, a pattern that warrants further observational testing.

While there are some hints of bending in the central and global properties of LTGs, larger-volume simulations are needed to explore the massive end of the mass function and to further in-

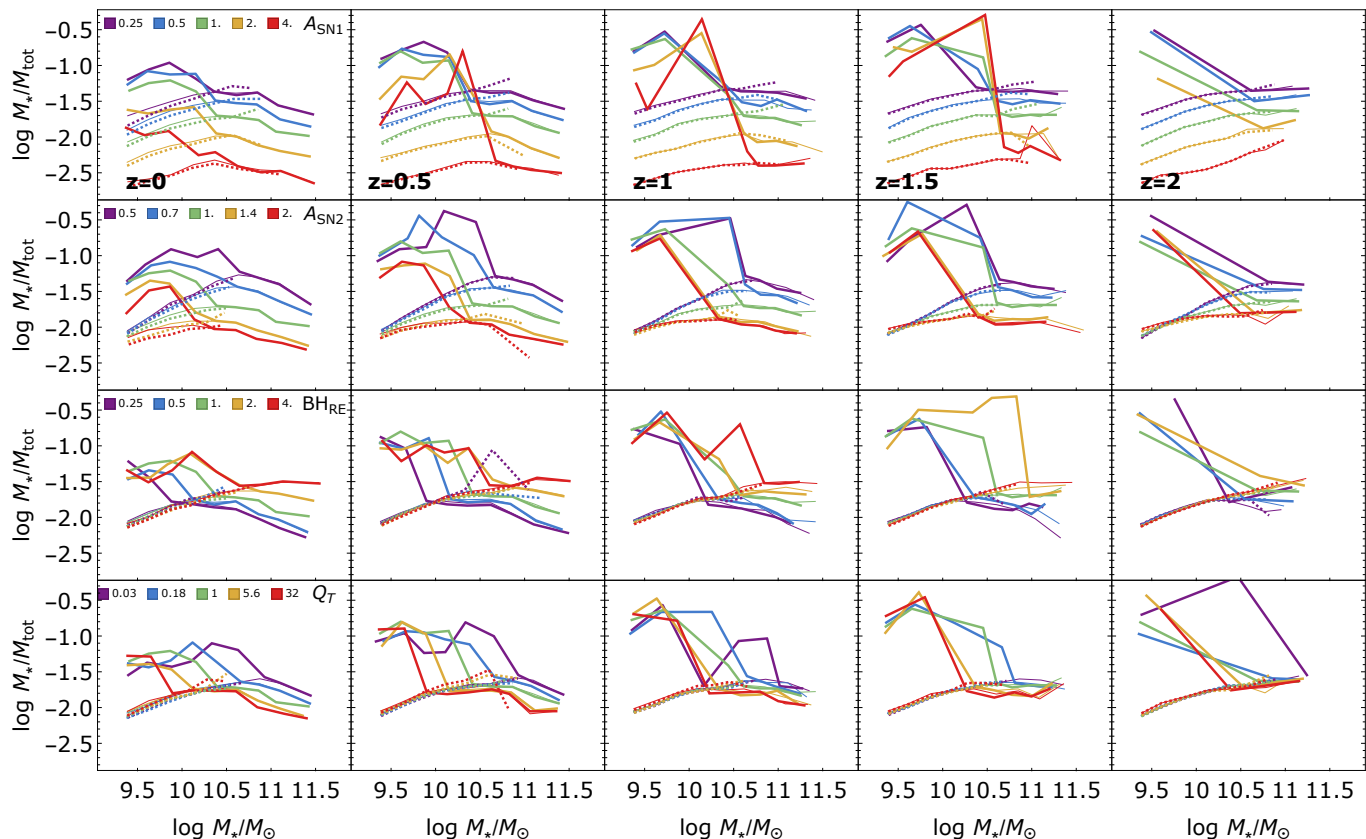


Fig. 6. The ratio M_*/M_{tot} is plotted against M_* , with rows showing variations in the two SN-related parameters A_{SN1} and A_{SN2} and two AGN parameters BH_{RE} and Q_T . The green lines represent the reference CAMELS simulation. Simulation snapshots at $z = 0$, $z = 0.5$, $z = 1$, $z = 1.5$ and $z = 2$ are displayed from left to right. The sample is divided in ETGs (solid lines) and LTGs (dashed lines). Thin lines are used for the median of the full sample. Medians in stellar mass bins are shown.

investigate the star formation efficiency in the most massive spiral galaxies (Posti et al. 2018; Tortora et al. 2019).

In future papers, following the procedure in Paper I and II, we will constrain these new simulations with such extended list of simulation parameters with observations (star forming galaxies: Tortora et al. 2019; passive galaxies: Tortora et al. 2012; Zhu et al. 2023), weighting the role of SN and AGN feedback. Among the new data available, the Euclid mission’s >100,000 strong lenses (Euclid Collaboration: Mellier et al. 2024; Acevedo Barroso et al. 2024), combined with weak lensing signals from stacked lenses and spectroscopic follow-ups (e.g. Collett et al. 2023), will provide precise data on central DM and total virial mass across a broad mass range and up to $z = 2$, allowing to constrain physical processes, and in particular AGN feedback (e.g. Mukherjee et al. 2019), which is one of the most dominant phenomena in very massive galaxies. Moreover, discovering several systems with spiral galaxies as lenses will also help address questions about the star formation efficiency of the most massive spiral galaxies across cosmic time, constraining the golden mass as a function of time and galaxy type.

Acknowledgements. C.T. and V.B. acknowledge the INAF grant 2022 LEMON.

References

Acevedo Barroso, J. A., O’Riordan, C. M., Clément, B., et al. 2024, arXiv e-prints, arXiv:2408.06217

- Benson, A. J., Cole, S., Frenk, C. S., Baugh, C. M., & Lacey, C. G. 2000, MNRAS, 311, 793
- Bisigello, L., Kuchner, U., Conselice, C. J., et al. 2020, MNRAS, 494, 2337
- Busillo, V., Tortora, C., Covone, G., et al. 2024, arXiv e-prints, arXiv:2412.00217
- Busillo, V., Tortora, C., Napolitano, N. R., et al. 2023, MNRAS, 525, 6191
- Capaccioli, M., Caon, N., & D’Onofrio, M. 1992, MNRAS, 259, 323
- Cappellari, M., McDermid, R. M., Alatalo, K., et al. 2013, MNRAS, 432, 1862
- Chabrier, G. 2003, PASP, 115, 763
- Chawak, C., Villaescusa-Navarro, F., Echeverri Rojas, N., et al. 2023, arXiv e-prints, arXiv:2309.12048
- Collett, T. E., Sonnenfeld, A., Frohmaier, C., et al. 2023, The Messenger, 190, 49
- Conroy, C. & Wechsler, R. H. 2009, ApJ, 696, 620
- Correa, C. A. & Schaye, J. 2020, MNRAS, 499, 3578
- Courteau, S., Cappellari, M., de Jong, R. S., et al. 2014, Reviews of Modern Physics, 86, 47
- Dekel, A. & Birnboim, Y. 2006, MNRAS, 368, 2
- D’Onofrio, M., Marziani, P., & Chiosi, C. 2021, Frontiers in Astronomy and Space Sciences, 8, 157
- Dutton, A. A., Conroy, C., van den Bosch, F. C., Prada, F., & More, S. 2010, MNRAS, 407, 2
- Euclid Collaboration: Mellier, Y., Abdurro’uf, Acevedo Barroso, J. A., et al. 2024, arXiv e-prints, arXiv:2405.13491
- Girelli, G., Pozzetti, L., Bolzonella, M., et al. 2020, A&A, 634, A135
- Hyde, J. B. & Bernardi, M. 2009, MNRAS, 394, 1978
- Kormendy, J., Fisher, D. B., Cornell, M. E., & Bender, R. 2009, ApJS, 182, 216
- Kuntschner, H., Emsellem, E., Bacon, R., et al. 2010, MNRAS, 408, 97
- Lelli, F., McGaugh, S. S., & Schombert, J. M. 2016, AJ, 152, 157
- Lovell, M. R., Pillepich, A., Genel, S., et al. 2018, MNRAS[arXiv:1801.10170]
- Marinoni, C. & Hudson, M. J. 2002, ApJ, 569, 101
- More, S., van den Bosch, F. C., Cacciato, M., et al. 2011, MNRAS, 410, 210
- Moster, B. P., Somerville, R. S., Maulbetsch, C., et al. 2010, ApJ, 710, 903

- Mukherjee, S., Koopmans, L. V. E., Metcalf, R. B., et al. 2018, *MNRAS*, 479, 4108
- Mukherjee, S., Koopmans, L. V. E., Metcalf, R. B., et al. 2019, arXiv e-prints [arXiv:1901.01095]
- Mukherjee, S., Koopmans, L. V. E., Metcalf, R. B., et al. 2021, *MNRAS*, 504, 3455
- Mukherjee, S., Koopmans, L. V. E., Tortora, C., et al. 2022, *MNRAS*, 509, 1245
- Napolitano, N. R., Capaccioli, M., Romanowsky, A. J., et al. 2005, *MNRAS*, 357, 691
- Napolitano, N. R., Romanowsky, A. J., & Tortora, C. 2010, *MNRAS*, 405, 2351
- Ni, Y., Genel, S., Anglés-Alcázar, D., et al. 2023, arXiv e-prints, arXiv:2304.02096
- Pillepich, A., Springel, V., Nelson, D., et al. 2018, *MNRAS*, 473, 4077
- Posti, L., Fraternali, F., & Marasco, A. 2018, arXiv e-prints [arXiv:1812.05099]
- Posti, L., Fraternali, F., & Marasco, A. 2019, *A&A*, 626, A56
- Rodríguez-Puebla, A., Avila-Reese, V., Yang, X., et al. 2015, *ApJ*, 799, 130
- Roy, N., Napolitano, N. R., La Barbera, F., et al. 2018, *MNRAS*, 480, 1057
- Sharma, G., Salucci, P., & van de Ven, G. 2022, *A&A*, 659, A40
- Shen, S., Mo, H. J., White, S. D. M., et al. 2003, *MNRAS*, 343, 978
- Spolaor, M., Kobayashi, C., Forbes, D. A., Couch, W. J., & Hau, G. K. T. 2010, *MNRAS*, 408, 272
- Toloba, E., Boselli, A., Cenarro, A. J., et al. 2011, *A&A*, 526, A114
- Tortora, C., La Barbera, F., & Napolitano, N. R. 2016, *MNRAS*, 455, 308
- Tortora, C., La Barbera, F., Napolitano, N. R., de Carvalho, R. R., & Romanowsky, A. J. 2012, *MNRAS*, 425, 577
- Tortora, C., Napolitano, N. R., Cardone, V. F., et al. 2010, *MNRAS*, 407, 144
- Tortora, C., Napolitano, N. R., Romanowsky, A. J., Capaccioli, M., & Covone, G. 2009, *MNRAS*, 396, 1132
- Tortora, C., Napolitano, N. R., Romanowsky, A. J., et al. 2011, *MNRAS*, 418, 1557
- Tortora, C., Napolitano, N. R., Roy, N., et al. 2018, *MNRAS*, 473, 969
- Tortora, C., Napolitano, N. R., Saglia, R. P., et al. 2014, *MNRAS*, 445, 162
- Tortora, C., Posti, L., Koopmans, L. V. E., & Napolitano, N. R. 2019, *MNRAS*, 489, 5483
- Tortora, C., Romanowsky, A. J., & Napolitano, N. R. 2013, *ApJ*, 765, 8
- Tully, R. B. & Verheijen, M. A. W. 1997, *ApJ*, 484, 145
- van den Bosch, F. C., Yang, X., Mo, H. J., et al. 2007, *MNRAS*, 376, 841
- Villaescusa-Navarro, F., Anglés-Alcázar, D., Genel, S., et al. 2021, *ApJ*, 915, 71
- Villaescusa-Navarro, F., Genel, S., Anglés-Alcázar, D., et al. 2022, arXiv e-prints, arXiv:2201.01300
- Widrow, L. M., Elahi, P. J., Thacker, R. J., Richardson, M., & Scannapieco, E. 2009, *Monthly Notices of the Royal Astronomical Society*, 397, 1275
- Wojtak, R. & Mamon, G. A. 2013, *MNRAS*, 428, 2407
- Wolf, J., Martinez, G. D., Bullock, J. S., et al. 2010, *MNRAS*, 406, 1220
- Zhu, K., Lu, S., Cappellari, M., et al. 2023, *MNRAS*, 522, 6326